Phase diagram of the Hubbard model on a honeycomb lattice: A cluster slave-spin study

Ming-Huan Zeng, Y.-J. Wang,* and Tianxing Ma†
Department of Physics, Beijing Normal University, Beijing 100875, China

(Received 27 September 2021; revised 20 January 2022; accepted 21 January 2022; published 31 January 2022)

The cluster slave-spin method is implemented to research the ground state properties of the honeycomb lattice Hubbard model with doping δ and coupling U being its parameters. At half filling, a single direct and continuous phase transition between the semimetal and antiferromagnetic (AFM) insulator is found at $U_{\mathrm{AFM}} = 2.43t$ that is in the Gross-Neveu-Yukawa universality class, where a relation between the staggered magnetization M and the AFM energy gap Δ_{AFM} is established as $M \propto \Delta_{\mathrm{AFM}}$, compared to $M \propto \Delta_{\mathrm{AFM}}(\ln \Delta_{\mathrm{AFM}})^2$ in the square lattice case. A first-order semimetal to the underlying paramagnetic (PM) insulator Mott transition is corroborated at $U_{\mathrm{Mott}} = 8.36t$, which is responsible for a broad crossover around $U_c = 5.4t$ between the weak- and strong-coupling regimes in the AFM state that increases with δ, in contrast to the square lattice case. In the doped system, the compressibility κ near the van Hove singularity at $\delta = 1/4$ is suppressed substantially by the interaction before the semimetal to AFM transition occurs, whereas κ near the Dirac points is very close to the noninteracting one, indicating that the Dirac cone structure of the energy dispersion is rather robust. An overall phase diagram in the U-δ plane is presented, consisting of four regimes: the AFM insulator at $\delta = 0$ for $U > U_{\mathrm{AFM}}$, the AFM metal with compressibility $\kappa > 0$ or $\kappa < 0$, and the PM semimetal; the AFM metal with $\kappa < 0$ only exists in an extremely small area near the phase boundary between the AFM and PM state.

DOI: 10.1103/PhysRevB.105.035155

I. INTRODUCTION

The Hubbard Hamiltonian [1] has been acting over decades as a prototypical model for the description of interacting electrons. In spite of its seeming simplicity, this model captures a rich phenomenology of strongly correlated electrons such as metallic-insulating, nonmagnetic-antiferromagnetic, and normal-superconducting phase transitions and cannot be solved exactly in more than one dimension, which necessitates some nonperturbative approaches to deal with the strong-coupling aspect of the model [2,3]. In this paper, we will focus on the one-band Hubbard model defined on a honeycomb (hexagon) network (Bravais lattice for graphene), which is bipartite and admits the antiferromagnetism (AFM) in the strong-coupling limit. This model has a linear free electron energy dispersion with nodal gapless points at the corners of the Brillouin zone, leading to the so-called Dirac semimetal. Due to the gapless Dirac points, there is a nontrivial semimetal to antiferromagnetic insulator (AFMI) transition at a finite coupling strength at half filling, which makes this model an ideal playground to research the interaction-driven semimetal to AFMI transition. Up till now, many numerical and analytical methods have been applied to the half-filled system to study this transition and its critical behaviors. Large-scale quantum Monte Carlo (QMC) simulations of 648 sites predict a spin liquid state in a range of interaction $3.5t < U < 4.3t$, beyond which the AFM sets in [4], and this argument was supported by some numerical works [5–8]. Nevertheless, this picture was disputed by many other numerical studies [9–17], especially those using the same method containing up to 2592 sites [9,15] and 20 808 sites [16,17]. By means of cluster dynamical mean-field theory, variational cluster approximation, and cluster dynamical impurity approximation, Hassan *et al.* [18] showed that the results are dependent on the shape and size of the clusters, and they claimed that only the system with two bath orbits per cluster boundary site is able to describe the correct behavior and found that the Mott transition for the spin liquid state is actually preempted by the AFM long-range order. Though the early variational cluster calculations [19] argued that the single-particle gap opens at an infinitesimal value of U, recent dynamical cluster approximation study found that this spurious excitation gap is due to the violation of the translation symmetry of the system and the cluster with one bath orbital per cluster site is sufficient for the description of the short-range correlations within the honeycomb unit cell [20]. A recent density matrix embedding theory study revealed a paramagnetic insulating state with possible hexagonal cluster state at intermediate coupling strength whose stability is highly cluster and lattice size dependent, and this state is nonexistent in the thermodynamic limit, signaling no intermediate state in the half-filled Hubbard model on a honeycomb lattice [21]. In addition, a two-particle self-consistent study presented a semimetal to AFMI transition and proved that the transition from a semimetal to spin liquid phase is forestalled by this transition [22]. The functional renormalization group theory predicts a critical interaction strength $U = 3.8t$ that is consistent with the results from the methods mentioned above, supporting that there is no spin liquid state at intermediate coupling strengths [23,24].

Based on the charge-spin separation theory [25–27], the $U(1)$ slave-spin method has been proposed to cope with the Mott transition in multiorbital systems [28], which is very

*yjwang@bnu.edu.cn
†txma@bnu.edu.cn

economical computationally because only $2M$ slave spins need to be introduced per site with M being the number of orbits. This method can not only reproduce the Gutzwiller factor $g_t = \frac{1-x-2d}{1-x-(1-x)^2/2}(\sqrt{x+d}+\sqrt{d})^2$, but also capture the right noninteracting behaviors at $U = 0$ because of an extra orbital-dependent chemical potential in the spinon Hamiltonian, which makes it a powerful method to deal with the strong-coupling systems [29]. Then, a cluster slave-spin approach was developed to address strongly correlated systems to take the short-range charge fluctuations into account [29] and has been employed to solve the square lattice Hubbard model to obtain an overall ground state phase diagram in the parameter space of doping δ and interaction U [30]. In the present work, we apply the same method with the Lanczos exact diagonalization as the slave-spin cluster solver to the honeycomb lattice Hubbard model to study its ground state properties, including the quantum critical behavior in the vicinity of the interaction-driven semimetal to AFMI transition at half filling and an overall phase diagram in the whole U-δ plane. Our motivation is twofold: (i) Because the results of this model are shown to be highly dependent on the size of the lattice adopted for QMC simulations, as well as the size and shape of the clusters used within various cluster approximations, more results from different approaches ought to be included and compared with each other. (ii) Away from half filling, much attention was paid to the $1/4$ doping, where the free density of states shows a van Hove singularity of logarithmic type, favoring an instability toward superconductivity in the weak-interaction regime [31–33], whereas an overall U-δ phase diagram pertaining to the magnetism is still absent.

In the honeycomb lattice Hubbard model, we find that the first-order Mott transition occurs at $U_{\text{Mott}} = 8.36t$ in the half-filled paramagnetic (PM) state, characterized by discontinuities and hystereses in all quantities, and transforms into a broad crossover in the AFM state because of long-range AFM correlations. Besides, the phase separation, manifested by a negative compressibility, has been observed in a region near the phase boundary $\delta_M(U)$ between the AFM and PM state and at intermediate couplings, whose area is much smaller compared to the square lattice Hubbard model [30]. Finally, a phase diagram in the U-δ plane is presented, consisting of four regimes: AFMI, AFM metal with positive and negative compressibility, and the PM semimetal.

The rest of this paper is organized as follows. In Sec. II, we reintroduce the cluster slave-spin mean-field theory [29,30] and implement it in the honeycomb lattice Hubbard model by making use of two- and six-site cluster approximations. In Sec. III A, for the half-filled system, an analytical relation between the staggered magnetization M and the AFM energy gap Δ_{AFM} in the vicinity of the semimetal to AFMI transition is established, and the first-order Mott transition at $U_{\text{Mott}} = 8.36t$ is observed in the PM state. In Sec. III B, the results of finite-doping cases obtained by two- and six-site clusters are discussed thoroughly, and we find that the two-site cluster is inadequate to capture the AFM transition appropriately because it violates the symmetry of the honeycomb lattice. In Sec. IV, the properties of M, Δ_{AFM}, and the compressibility κ are combined to show a phase diagram of the model in the U-δ plane.

II. FORMALISM

The standard one-band fermionic Hubbard model [1] reads

$$H = -t\sum_{\langle i,j\rangle\sigma}(c^\dagger_{i\sigma}c_{j\sigma} + \text{H.c.}) + U\sum_i n_{i\uparrow}n_{i\downarrow} - \mu\sum_{i\sigma} n_{i\sigma}, \tag{1}$$

where t, U, μ are the nearest hopping constant, the on-site Coulomb repulsion energy, and the chemical potential, respectively. The sum $\langle i, j\rangle$ runs over all pairs of nearest-neighbor sites on a honeycomb lattice, and $c^\dagger_{i\sigma}$ is the creation operator of the electron at site i with spin $\sigma =\uparrow, \downarrow$, and the number operator $n_{i\sigma} = c^\dagger_{i\sigma}c_{i\sigma}$. Hereafter, we use $t = 1$ as the unit of energy.

In the $U(1)$ slave-spin method [28], an electron operator is factorized into a slave-spin operator ($S = \frac{1}{2}$) and a fermionic spinon operator, describing the charge and spin degrees of freedom of an electron, respectively:

$$c^\dagger_\alpha \equiv S^\dagger_\alpha f^\dagger_\alpha, \tag{2}$$

on account of which the original Hilbert space with basis $\{|0\rangle, |1\rangle\}$ is enlarged to $\{|n^f_\alpha, S^z_\alpha\rangle\} = \{|0, -\frac{1}{2}\rangle, |1, \frac{1}{2}\rangle, |0, \frac{1}{2}\rangle, |1, -\frac{1}{2}\rangle\}$. Thus, an extra constraint needs to be imposed to restrict the Hilbert space to the physical one: $\{|n^f_\alpha, S^z_\alpha\rangle\} = \{|0, -\frac{1}{2}\rangle, |1, \frac{1}{2}\rangle\}$,

$$S^z_\alpha = f^\dagger_\alpha f_\alpha - \tfrac{1}{2}. \tag{3}$$

A gauge degree of freedom must be introduced to incorporate the constraint, signifying that the slave-spin representation is invariant under a local gauge transformation $f^\dagger_\alpha \to f^\dagger_\alpha e^{-i\phi_\alpha}$ and $S^\dagger_\alpha \to S^\dagger_\alpha e^{i\phi_\alpha}$, and all physical quantities should be invariant under this $U(1)$ gauge transformation [26,34–37].

With the constraint $a^\dagger_\alpha a_\alpha + b^\dagger_\alpha b_\alpha = 1$, the slave-spin operator is rewritten in the Schwinger boson representation

$$S^\dagger_\alpha = a^\dagger_\alpha b_\alpha, \quad S^z_\alpha = \tfrac{1}{2}(a^\dagger_\alpha a_\alpha - b^\dagger_\alpha b_\alpha). \tag{4}$$

To ensure the correct noninteracting behaviors, the slave-boson operators need to be dressed as follows [38]:

$$\tilde{S}^\dagger_\alpha = P^+_\alpha a^\dagger_\alpha b_\alpha P^-_\alpha, \tag{5a}$$

$$P^\pm_\alpha = \frac{1}{\sqrt{1/2 \pm S^z_\alpha}}, \tag{5b}$$

which can be linearized as follows:

$$\tilde{S}^\dagger_\alpha \approx \tilde{z}^\dagger_\alpha + \frac{\langle\tilde{z}^\dagger_\alpha\rangle\langle S^z_\alpha\rangle\Delta S^z_\alpha}{\left(\frac{1}{2}\right)^2 - \langle S^z_\alpha\rangle^2}, \tag{6}$$

with $\Delta S^z_\alpha = S^z_\alpha - \langle S^z_\alpha\rangle$ and $\tilde{z}^\dagger_\alpha = a^\dagger_\alpha b_\alpha/[(\frac{1}{2})^2 - \langle S^z_\alpha\rangle^2]^{1/2}$.

Following the recipe of Lee and Lee [29], with the local constraints (3) being ensured roughly by two global Lagrange multipliers $\lambda_{I\sigma}$ on sublattices $I = A$ and B, Hamiltonian (1)

can be cast into the form

$$H^f_{\rm MF} = -tZ\sum_{\langle i,j\rangle\sigma}(a^\dagger_{i\sigma}b_{j\sigma}+{\rm H.c.}) - \sum_{i\sigma}[(\mu+\lambda_{A\sigma}-\tilde{\mu}_{A\sigma})a^\dagger_{i\sigma}a_{i\sigma} +(\mu+\lambda_{B\sigma}-\tilde{\mu}_{B\sigma})b^\dagger_{i\sigma}b_{i\sigma}], \tag{7a}$$

$$H^S_{n_c\text{-site}} = H^\lambda_{n_c\text{-site}} + H^U_{n_c\text{-site}} + H^K_{n_c\text{-site}}, \tag{7b}$$

where

$$H^\lambda_{n_c\text{-site}} = \sum_{i_c=1,\sigma}^{n_c}\lambda_{I\sigma}S^z_{i_c\sigma}, \tag{8a}$$

$$H^U_{n_c\text{-site}} = \sum_{i_c=1}^{n_c}U\left(S^z_{i_c\sigma}+\frac{1}{2}\right)\left(S^z_{i_c\bar{\sigma}}+\frac{1}{2}\right), \tag{8b}$$

$$H^K_{2\text{-site}} = \sum_\sigma\left\{\epsilon^{\delta_1}_\sigma(\tilde{z}^\dagger_{A\sigma}\tilde{z}_{B\sigma}+\tilde{z}^\dagger_{B\sigma}\tilde{z}_{A\sigma})+\left(\epsilon^{\delta_2}_\sigma+\epsilon^{\delta_3}_\sigma\right) \times[\tilde{z}^\dagger_{A\sigma}\langle\tilde{z}_{B\sigma}\rangle+\tilde{z}^\dagger_{B\sigma}\langle\tilde{z}_{A\sigma}\rangle+{\rm H.c.}]\right\}, \tag{8c}$$

$$\begin{aligned}H^K_{6\text{-site}} = \sum_\sigma\Big\{&\epsilon^{\delta_1}_\sigma(\tilde{z}^\dagger_{1\sigma}\tilde{z}_{2\sigma}+\tilde{z}^\dagger_{4\sigma}\tilde{z}_{5\sigma})\\&+\epsilon^{\delta_2}_\sigma(\tilde{z}^\dagger_{1\sigma}\tilde{z}_{6\sigma}+\tilde{z}^\dagger_{3\sigma}\tilde{z}_{4\sigma})+\epsilon^{\delta_3}_\sigma(\tilde{z}^\dagger_{2\sigma}\tilde{z}_{3\sigma}+\tilde{z}^\dagger_{5\sigma}\tilde{z}_{6\sigma})\\&+\epsilon^{\delta_1}_\sigma(\tilde{z}^\dagger_{3\sigma}\langle\tilde{z}_{6\sigma}\rangle+\langle\tilde{z}^\dagger_{3\sigma}\rangle\tilde{z}_{6\sigma})\\&+\epsilon^{\delta_2}_\sigma(\tilde{z}^\dagger_{2\sigma}\langle\tilde{z}_{5\sigma}\rangle+\langle\tilde{z}^\dagger_{2\sigma}\rangle\tilde{z}_{5\sigma})\\&+\epsilon^{\delta_3}_\sigma(\tilde{z}^\dagger_{1\sigma}\langle\tilde{z}_{4\sigma}\rangle+\langle\tilde{z}^\dagger_{1\sigma}\rangle\tilde{z}_{4\sigma})+{\rm H.c.}\Big\}.\end{aligned} \tag{8d}$$

The mean-field Hamiltonian $H^S_{n_c\text{-site}}$ is a Bose-Hubbard model for two species of bosons, and actually a model of interacting XY spins in a magnetic field [28]. Senthil has systematically investigated the gauge field fluctuations' effects on charge and spin degrees of freedom of the one-band Hubbard model in the slave-rotor representation [36], which is very similar to the slave-spin method adopted in this paper. He found that [37] the dynamical exponent $z=1$ at the mean-field critical fixed point renders that the Landau damping term of the gauge bosons, $|\omega|/q$, scales as a Higgs mass term. Hence, for the rotors, the gauge bosons are gapped and harmless, indicating that the universality class of the rotor quantum critical point remains unaltered from the 3D XY model [39]. In this paper, the gauge fluctuations will not be considered further on the same ground.

The cluster slave-spin Hamiltonian (7b) with $n_c=2$, 6, marked by the red color geometry in Fig. 1, will be solved by using the Lanczos exact-diagonalization method. The parameters Z, $\tilde{\mu}_{I\sigma}$, and ϵ^δ_σ in Eqs. (7) and (8) are calculated as follows:

$$Z=\langle\tilde{z}^\dagger_{A\sigma}\rangle\langle\tilde{z}_{B\sigma}\rangle,\quad \epsilon^{\delta_{1/2/3}}_\sigma=-t\langle a^\dagger_{i\sigma}b_{i+\hat{\delta}_{1/2/3}\sigma}\rangle,$$
$$\tilde{\mu}_{I\sigma}=\frac{2Z\langle S^z_{I\sigma}\rangle\left(\epsilon^{\delta_1}_\sigma+\epsilon^{\delta_2}_\sigma+\epsilon^{\delta_3}_\sigma\right)}{\left(\frac{1}{2}\right)^2-\langle S^z_{I\sigma}\rangle^2}. \tag{9}$$

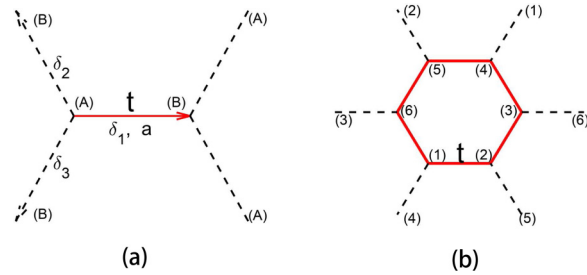

FIG. 1. Schematic illustration of the (a) two- and (b) six-site cluster configurations. The lattice constant a is set to unity, and the positions of three nearest neighbors of site A are $\delta_1=(1,0)$, $\delta_2=(-1/2,\sqrt{3}/2)$, $\delta_3=-(1/2,\sqrt{3}/2)$.

Moreover, the fermionic spinon Hamiltonian can be Fourier transformed into momentum space:

$$H^f_{\rm MF}=\sum_{\boldsymbol{k},\sigma}(\varepsilon_{A\sigma}a^\dagger_{\boldsymbol{k}\sigma}a_{\boldsymbol{k}\sigma}+\varepsilon_{B\sigma}b^\dagger_{\boldsymbol{k}\sigma}b_{\boldsymbol{k}\sigma} +\Gamma_{\boldsymbol{k}}a^\dagger_{\boldsymbol{k}\sigma}b_{\boldsymbol{k}\sigma}+\Gamma^*_{\boldsymbol{k}}b^\dagger_{\boldsymbol{k}\sigma}a_{\boldsymbol{k}\sigma}) \tag{10}$$

with

$$\varepsilon_{A/B\sigma}=\tilde{\mu}_{A/B\sigma}-\mu-\lambda_{A/B\sigma},$$
$$\Gamma_{\boldsymbol{k}}=-tZ\gamma_{\boldsymbol{k}},\quad \gamma_{\boldsymbol{k}}=\sum_{\boldsymbol{\delta}}e^{i\boldsymbol{k}\cdot\boldsymbol{\delta}}. \tag{11}$$

Diagonalization of the spinon Hamiltonian (10) gives rise to the eigenenergies as

$$E^\pm_{\boldsymbol{k}}=\pm\sqrt{|\Gamma_{\boldsymbol{k}}|^2+\Delta^2_\sigma}-\mu_{\rm eff}, \tag{12a}$$

$$\mu_{\rm eff}=\mu-\tfrac{1}{2}(\tilde{\mu}_{A\sigma}-\lambda_{A\sigma}+\tilde{\mu}_{B\sigma}-\lambda_{B\sigma}), \tag{12b}$$

$$\Delta_\sigma=\tfrac{1}{2}(\tilde{\mu}_{A\sigma}-\lambda_{A\sigma}-\tilde{\mu}_{B\sigma}+\lambda_{B\sigma}). \tag{12c}$$

Here, the AFM energy gap $\Delta_{\rm AFM}=|\Delta_\sigma|$ is identical in form to that in the square lattice case [29,30].

In most occasions, it proves effective to adopt the density of states (DOS) of the noninteracting electrons to calculate the physical quantities in the thermodynamic limit. On the honeycomb lattice, it is defined as

$$D(\gamma)=\frac{1}{\mathcal{N}_{\rm triangle}}\sum_{\boldsymbol{k}}\delta(\gamma-|\gamma_{\boldsymbol{k}}|) =\begin{cases}N(\gamma), & 0\leqslant\gamma<1,\\ \tilde{N}(\gamma), & 1<\gamma\leqslant 3,\end{cases} \tag{13}$$

where $\mathcal{N}_{\rm triangle}$ is the site number of the underlying triangular lattice, which is half of that of the honeycomb lattice, and

$$N(\gamma)=\frac{4}{\pi^2}\frac{\gamma}{\sqrt{(3-\gamma)(1+\gamma)^3}}K\left(\sqrt{\frac{16\gamma}{(3-\gamma)(1+\gamma)^3}}\right),$$
$$\tilde{N}(\gamma)=\frac{1}{\pi^2}\sqrt{\gamma}\,K\left(\sqrt{\frac{(3-\gamma)(1+\gamma)^3}{16\gamma}}\right), \tag{14}$$

with $K(x)$ being the complete elliptic integral of the first kind. In comparison to the self-dual situation on a square lattice, we

now have a duality transformation

$$\tilde{\gamma} = \frac{3-\gamma}{1+\gamma} \tag{15}$$

to connect these two parts, under which

$$\frac{(3-\tilde{\gamma})(1+\tilde{\gamma})^3}{16\tilde{\gamma}} = \frac{16\gamma}{(3-\gamma)(1+\gamma)^3}, \tag{16a}$$

$$\frac{(3-\tilde{\gamma})(1+\tilde{\gamma})}{4\tilde{\gamma}} = \frac{4\gamma}{(3-\gamma)(1+\gamma)}, \tag{16b}$$

and

$$\begin{aligned}\tilde{N}(\gamma) &= \frac{(3-\tilde{\gamma})(1+\tilde{\gamma})}{4\tilde{\gamma}} N(\tilde{\gamma}) \\ &= \frac{4\gamma}{(3-\gamma)(1+\gamma)} N\left(\frac{3-\gamma}{1+\gamma}\right).\end{aligned} \tag{17}$$

Then, the self-consistent quantities $\epsilon_\sigma^\delta = \epsilon$ and $n_{(A/B)\sigma} \equiv \langle a_{i\sigma}^\dagger a_{i\sigma}\rangle / \langle b_{i\sigma}^\dagger b_{i\sigma}\rangle$ can be calculated through

$$\epsilon = \int_0^3 d\gamma\, D(\gamma) \frac{(tZ\gamma)^2}{6Z\sqrt{(tZ\gamma)^2+\Delta^2}} \sum_{s=\pm} s\theta[-E^s(\gamma)], \tag{18}$$

$$\begin{aligned}n_{(A/B)\sigma} &= \int_0^3 d\gamma\, D(\gamma) \sum_{s=\pm} \theta[-E^s(\gamma)] \\ &\times \frac{1}{2}\left(1 \pm s\frac{\Delta_\sigma}{\sqrt{(tZ\gamma)^2+\Delta^2}}\right),\end{aligned} \tag{19}$$

where $E^\pm(\gamma) = \pm\sqrt{(tZ\gamma)^2+\Delta^2} - \mu_{\text{eff}}$ and $\Delta_\sigma^2 = \Delta^2$.

III. RESULTS AND DISCUSSION

A. Half-filled system

In this case, the particle-hole symmetry implies $\mu_{\text{eff}} = 0$ and $E^+(\gamma) > 0$, and by relation (3), Eqs. (18) and (19) are simply

$$\epsilon = -\frac{t\lambda}{6} I_\epsilon(\lambda), \tag{20}$$

$$\left\langle S^z_{(A/B)\sigma}\right\rangle = (-/+)\frac{\text{sgn}(\Delta_\sigma)}{2} I_S(\lambda), \tag{21}$$

where $\lambda = tZ/\Delta_{\text{AFM}}$ and

$$I_\epsilon(\lambda) = \int_0^3 d\gamma\, D(\gamma) \frac{\gamma^2}{\sqrt{(\gamma\lambda)^2+1}}, \tag{22}$$

$$I_S(\lambda) = \int_0^3 d\gamma\, D(\gamma) \frac{1}{\sqrt{(\gamma\lambda)^2+1}}. \tag{23}$$

For the half-filled square lattice Hubbard model at $T = 0$, the AFM order emerges for any nonzero U because of the perfect nesting of the free Fermi surface, whereas the honeycomb lattice is known to have a semimetal phase at small U due to the low coordination number which allows more fluctuations and an antiferromagnetic phase at large U. It is well established that there is a single direct and continuous phase transition from semimetal to AFMI at a finite critical interaction strength U_{AFM} for the half-filled honeycomb lattice Hubbard model.

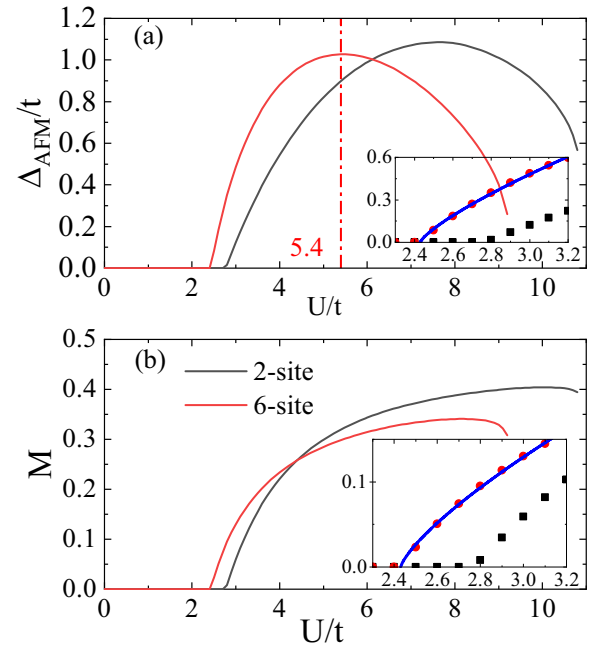

FIG. 2. (a) The AFM energy gap Δ_{AFM} and (b) the staggered magnetization M as function of U, where the insets show the same data in the vicinity of the critical coupling together with the fitting data (blue lines). The results from two-site cluster approximation are presented as well (black).

This U_{AFM} from large-scale QMC simulations mainly locates around $U \approx 3.8$ [9–11,15,17,40], whereas the results from various cluster scenarios, such as cluster dynamical impurity approximation, variational cluster approximation, dynamical cluster approximation, and density matrix embedding theory, are strongly cluster dependent and the U'_{AFM}s are in a wide range of $1.5 \lesssim U \lesssim 4.0$ [13,18–21]. As shown in Fig. 2, we find that $U_{\text{AFM}} = 2.75$ or 2.43 in our two- or six-site cluster approximation, which is larger than that from the Hartree-Fock approximation of 2.235 [10,14], but smaller than those from QMC simulations [9,11,15,17,40], reflecting the fact that fluctuations have been incorporated in the six-site cluster, but not enough to give the accurate value. This shortcoming may be remedied by enlarging the cluster size and strictly dealing with the constraint $S^z_\alpha = f^\dagger_\alpha f_\alpha - \frac{1}{2}$ locally. However, the two-site cluster value of U_{AFM} is larger than that from the six-site cluster, necessitating more investigations on the dependence of U_{AFM} upon the cluster size. To extract the critical information around U_{AFM}, we fit our self-consistent data from the six-site cluster using the U-dependent form of M and Δ_{AFM} that have been verified by QMC simulations [9,11,15,17] and density matrix embedding theory [21],

$$\Delta_{\text{AFM}}/M = \alpha_{1/2}|U - U_{\text{AFM}}|^{\beta_{1/2}}, \tag{24}$$

and we obtain

$$\begin{aligned}&\alpha_1 = 0.74021 \pm 0.00836, \quad \beta_1 = 0.77086 \pm 0.01597; \\ &\alpha_2 = 0.19739 \pm 0.000753, \quad \beta_2 = 0.755 \pm 0.0049.\end{aligned} \tag{25}$$

The critical exponent $\beta_2 = 0.755 \pm 0.0049$ for M is very close to $\beta_2 = 0.75 \pm 0.06$ [9] and 0.79 [11] from the large-scale QMC simulations, and $\beta_2 = 0.72$ from the density

embedding theory [21]. It should be mentioned that $\beta_2 = 0.86546 \pm 0.01849$ from the two-site approximation is close to that from the six-site one, and both results fall in the ballpark of the QMC estimates, reflecting the universal aspect of the critical exponent. The critical exponent for single particle gap $\Delta_{\rm AFM}$ is slightly larger than that of M [11,17].

We now expand asymptotically the integrals $I_\epsilon(\lambda)$ and $I_S(\lambda)$ defined in Eqs. (22) and (23) as $\lambda \to \infty$ [41]:

$$\epsilon = -\frac{t}{6}\left(1.574597 - 0.448221\tilde{\Delta}^2 + \frac{4}{3\sqrt{3}\pi}\tilde{\Delta}^3 + \cdots\right), \tag{26}$$

$$\left\langle S^z_{(A/B)\sigma}\right\rangle = (-/+)\frac{\mathrm{sgn}(\Delta_\sigma)}{2}\left(0.896441\tilde{\Delta} - \frac{2}{\sqrt{3}\pi}\tilde{\Delta}^2 - 0.014\tilde{\Delta}^3 + \frac{4}{9\sqrt{3}\pi}\tilde{\Delta}^4 + \cdots\right), \tag{27}$$

where $\tilde{\Delta} = \lambda^{-1} = \Delta_{\rm AFM}/tZ$. The relation between M and $\Delta_{\rm AFM}$ in the honeycomb lattice around $U = U_{\rm AFM}$ is established as

$$M = \frac{1}{2}\left|\left\langle S^z_{A\sigma}\right\rangle - \left\langle S^z_{B\sigma}\right\rangle\right| \approx \frac{1}{2}\left(0.896441\tilde{\Delta} - \frac{2}{\sqrt{3}\pi}\tilde{\Delta}^2 - 0.014\tilde{\Delta}^3 + \frac{4}{9\sqrt{3}\pi}\tilde{\Delta}^4\right). \tag{28}$$

To the leading order, $M \propto \Delta_{\rm AFM}$, compared to $M \propto \Delta_{\rm AFM}(\ln \Delta_{\rm AFM})^2$ in the square lattice, supporting the AFM at small U in the latter case is driven by the perfect nesting of its free Fermi surface.

On the other hand, $\Delta_{\rm AFM}$ reaches its maximum around the crossover coupling strength $U_c = 5.4t$ that separates the weak- and strong-coupling regimes, which is consistent with the traditional mean-field behavior $\Delta_{\rm AFM} \sim U$ at small U, and $\Delta_{\rm AFM} \sim 4t^2/U$ in the large-U limit supported by the superexchange mechanism. It ought to be mentioned that M drops abruptly when U is larger than a certain value where the quasiparticle weight happens to drop to zero as shown in Fig. 3(a), implying that at half filling, the cluster slave-spin method is incapable of capturing the crossover between the Hubbard model with finite U and its counterpart in the large-U limit—the Heisenberg model, which can be understood from the expression of M at half filling,

$$M = \frac{1}{2}|n_{A\sigma} - n_{B\sigma}| = \int_0^3 d\gamma\, D(\gamma)\frac{|\Delta_\sigma|}{\sqrt{(tZ\gamma)^2 + \Delta^2}}, \tag{29}$$

where the integration encounters $\frac{0}{0}$ when the AFM energy gap $\Delta_{\rm AFM}$ and the quasiparticle residue Z drop to zero simultaneously at large U [see Figs. 2(a) and 3(a)]. However, for a doped system, Z decreases to a constant [Fig. 4(a)] to be free from this glitch.

The quasiparticle residue Z, the generalized Gutzwiller factor g_t [29,42,43], the holon-doublon correlators C_{ij} [29] between the nearest neighbors C_{12}, the next-nearest neighbors C_{13}, and the next-next-nearest neighbors C_{14}, the ground state energy of the slave-spin Hamiltonian per site $\langle H^S_{n_c\text{-site}}\rangle/n_c$ with n_c being the cluster size, and the double occupancy $\langle D\rangle$ as function of U at half filling obtained from two- and six-site cluster approximations are presented in Fig. 3, where C_{ij} is

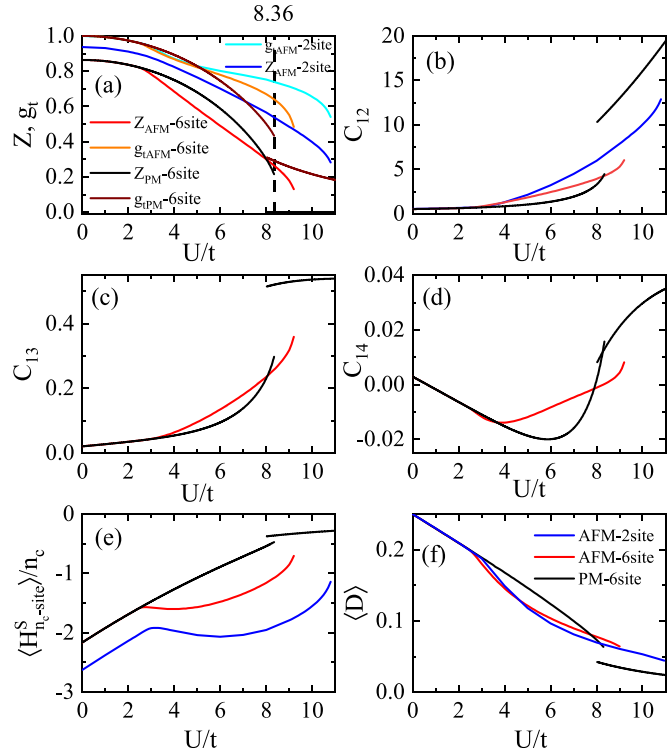

FIG. 3. (a) The quasiparticle weight Z and the generalized Gutzwiller factor g_t. (b)–(d) The holon-doublon correlators between the nearest neighbors C_{12}, the next-nearest neighbors C_{13}, and the next-next-nearest neighbors C_{14}. (e) The expectation value of the cluster slave-spin Hamiltonian $\langle H^S_{n_c\text{-site}}\rangle/n_c$. (f) The double occupancy $\langle D\rangle$ in the AFM state vs U obtained by the 2/6-site clusters (blue/red). All quantities in the PM state obtained by 6-site cluster are black lines.

defined as

$$C_{ij} = \frac{\langle N_i D_j\rangle - \langle N_i\rangle\langle D_j\rangle}{\langle N_i\rangle\langle D_j\rangle}, \tag{30}$$

with the holon operator $N_i = (1 - n_{i\sigma})(1 - n_{i\bar{\sigma}})$ and doublon operator $D_j = n_{j\sigma}n_{j\bar{\sigma}}$.

The results are as follows: (i) All quantities in the PM state show discontinuities and hystereses at the critical coupling strength $U_{\rm Mott} = 8.36$ for the semimetal to paramagnetic insulator transition as the characteristics of the first-order Mott transition in the PM state [18,44]. (ii) In Fig. 3(a), compared to that in the PM state, Z is largely suppressed as entering the AFM phase. (iii) In Figs. 3(b)–3(d), C_{12} and C_{13} are positive and increase monotonically with U, signaling that the holon and doublon between the nearest and next-nearest neighbors tend to attract each other, which is enhanced by the coupling strength. However, C_{14} presents a negative minimum beyond the AFM transition or as U approaches $U_{\rm Mott}$ in the PM state, suggesting that at half filling, the holon and doublon between the next-next-nearest neighbors attract each other when U is small or large, while they behave repulsively at intermediate U. (iv) In Fig. 3(e), $\langle H^S_{n_c\text{-site}}\rangle/n_c$ in the AFM state is smaller than that from the PM state, favoring an AFM ground state. (v) In Fig. 3(f), $\langle D\rangle$ in the PM state decreases linearly with the increasing U when $U \ll U_{\rm Mott}$ [45], whereas in the AFM

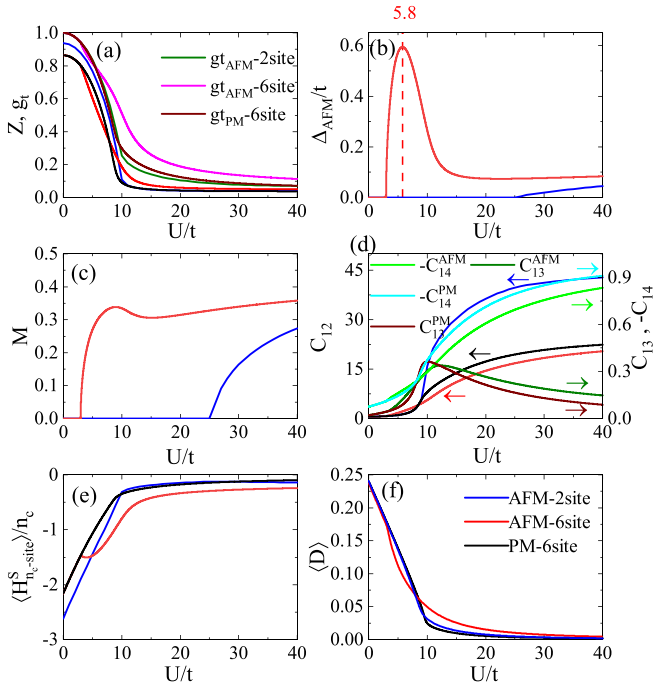

FIG. 4. (a) The quasiparticle weight Z and the generalized Gutzwiller factor g_t, (b) the AFM energy gap Δ_{AFM}/t, (c) the staggered magnetization M, (d) the holon-doublon correlators between the nearest neighbors C_{12}, the next-nearest neighbors C_{13}, and the next-next-nearest neighbors C_{14}, (e) the expectation value of the cluster slave-spin Hamiltonian $\langle H^S_{n_c\text{-site}}\rangle/n_c$, and (f) the double occupancy $\langle D\rangle$ as function of U at $\delta = 0.02$ in the AFM state obtained by the two-site (blue) and six-site (red) cluster, as well as the PM state (black) by six-site cluster.

state, its slope changes abruptly as AFM sets in denoting a second-order transition from a semimetal to an AFMI.

B. Systems with finite doping

In Fig. 4, we plot Z, g_t, Δ_{AFM}, M, $C_{12/3/4}$, $\langle H^S_{n_c\text{-site}}\rangle/n_c$, $\langle D\rangle$ as functions of U at $\delta = 0.02$ obtained from two- and six-site cluster approximations to further compare the results from these two slave-spin clusters. In Fig. 4(a), the quasiparticle residue from six-site cluster is much smaller than that from two-site because of more quantum fluctuations, and becomes flattened when $U > U_{\mathrm{Mott}}$. In Fig. 4(b), the critical coupling strength for the AFM transition from the six-site cluster is $U_{\mathrm{AFM}} = 3.0$, while that from the two-site cluster locates at $U_{\mathrm{AFM}} = 25.0$, which indicates that the two-site cluster is inadequate to describe the AFM transition in the honeycomb lattice because it does not keep track of the lattice symmetry. In Fig. 4(d), C_{12} increases slowly when $U < U_{\mathrm{Mott}}$, then rises dramatically as U approaches U_{Mott}, and finally grows progressively as U goes to infinity, while C_{13} shows a maximum near U_{Mott}, the reason for which is that the hopping probability between the next-nearest neighbors falls faster than the one between the nearest neighbors when U is increased as demonstrated in our previous work on a square lattice [30]. Unlike C_{12} and C_{13}, both positive for all U's, C_{14} is negative at $\delta = 0.02$ and its magnitude grows monotonically with the coupling strength, indicating that the holon and doublon

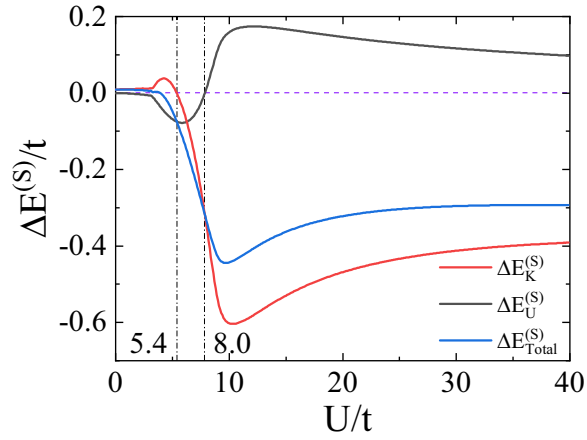

FIG. 5. The difference of the kinetic energy $\Delta E_K^{(S)}$ (red), interaction potential $\Delta E_U^{(S)}$ (black), and their summation $\Delta E_{\mathrm{Total}}^{(S)}$ (blue) of the six-site cluster slave-spin Hamiltonian Eq. (8d) between the AFM and PM states as function of U at $\delta = 0.02$.

between the next-next-nearest neighbors repulse each other, whose tendency is strengthened as U increases. In Fig. 4(e), as shown by the blue line with $0 < U < 25$ (where the system within the two-site approximation is in the PM state) and the black line, the difference of $\langle H^S_{n_c\text{-site}}\rangle/n_c$ in the PM state between the two- and six-site cluster approximations is much smaller when $U > U_{\mathrm{Mott}}$, denoting that the cluster size's effect on the properties of the system in the PM state is less important at large U as the system becomes more localized, where the intersite fluctuations are much weaker in contrast to the weak-coupling limit. In Fig. 4(f), there exists an inflection in $\langle D\rangle$ in the PM state around $U \approx 10t$, meaning that the first-order Mott transition at half filling turns into a continuous crossover at finite dopings. For $U < 8.0$, the double occupancy in the AFM state is smaller than that in the PM state while the opposite is true for $U > 8.0$, bespeaking that the AFM at small U is triggered by the interaction potential gain while that in the large-U limit is not driven by this mechanism. This picture can also be seen in Fig. 5, where there exists a region ($5.4 < U < 8.0$) with $\Delta E_U^{(S)} < 0$ and $\Delta E_K^{(S)} < 0$, signaling that the AFM in this region is supported by both the kinetic energy and interaction potential gain. The dependence of the quantities discussed above upon the interaction strength at various dopings of $\delta = 0.02, 0.0375, 0.1, 0.1531, 0.1725$ obtained through six-site cluster approximation are presented in Fig. 6, where $\delta = 0.1531$ is the critical doping for the AFM to PM phase transition at $U = 40$, and $\delta = 0.1725$ is the maximum of δ_M, i.e., the boundary between the AFM and PM state (see Figs. 8 and 11). The following results are concluded: (i) In Fig. 6(a), the increasing Z with δ for all coupling strengths suggests that the system with the increasing doping tends to be metallic. When $U > U_{\mathrm{Mott}}$, the quasiparticle residues decrease progressively to constants, manifesting that the properties in the AFM state are controlled by the underlying Mott transition. (ii) In Fig. 6(b), Δ'_{AFM}s at all dopings exhibit a maximum around the crossover coupling strength $U_c(\delta)$ that grows with δ. (iii) In Fig. 6(d), C_{12} increases monotonically with U at all dopings and diminishes as δ goes up, which makes it eligible to be an indicator of the magnitude of correlations.

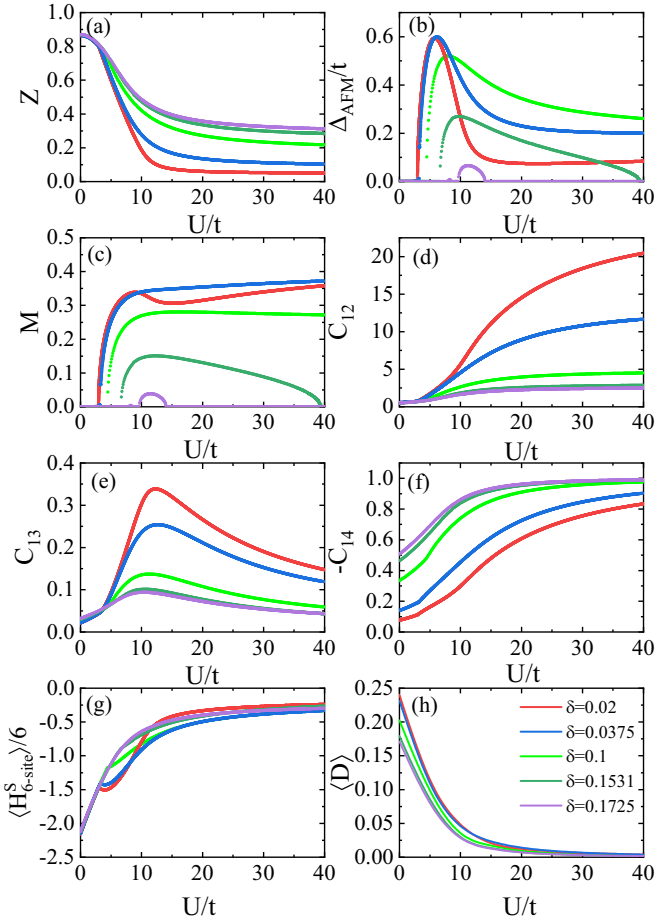

FIG. 6. (a) The quasiparticle weight Z, (b) the AFM energy gap Δ_{AFM}/t, (c) the staggered magnetization M, (d)–(f) the holon-doublon correlator between the nearest neighbors C_{12}, the next-nearest neighbors C_{13}, and the next-next-nearest neighbors C_{14}, (g) the expectation value of the cluster slave-spin Hamiltonian, and (h) the double occupancy $\langle D\rangle$ as function of U at a series of doping concentrations $\delta = 0.02$ (red), 0.0375 (blue), 0.1 (green), 0.1531 (dark green), 0.1725 (violet) in the AFM state obtained by the six-site cluster.

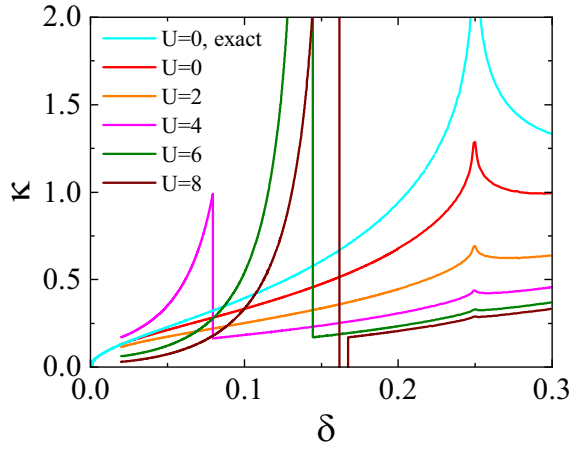

FIG. 7. The compressibility κ obtained from the six-site cluster approximation as function of δ at $U = 0, 2, 4, 6, 8$ (red, orange, magenta, olive, brown, respectively), and the exact one at $U = 0$ calculated through Eq. (31) (cyan).

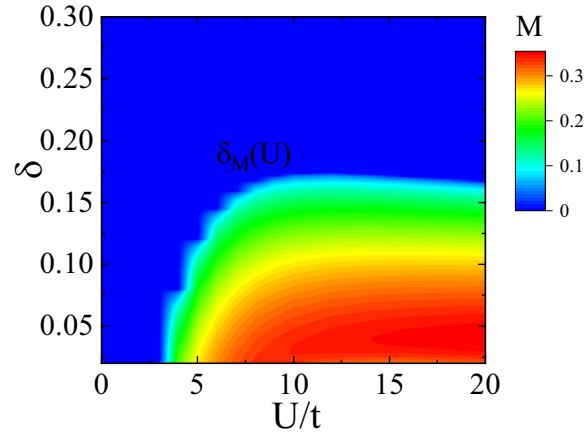

FIG. 8. The staggered magnetization M as function of U and δ obtained by six-site cluster, where $\delta_M(U)$ is the phase boundary between the AFM and PM states.

(iv) In Fig. 6(g), compared to the PM state, $\langle H^S_{6\text{-site}}\rangle/6$ is suppressed dramatically as soon as AFM sets in and this effect is weakened by the increasing δ.

The compressibility of the system is defined as $\kappa = n^{-2}\partial n/\partial\mu$. At $U = 0$, it is calculated by using the noninteracting DOS $D(\gamma)$, Eq. (13), via

$$\kappa(\mu) = \begin{cases} \dfrac{N(|\mu|)}{\left[\frac{3}{4}+\int_{-1}^{\mu} N(|\gamma|)d\gamma\right]^2}, & 0 < \delta < \frac{1}{4}, \\ \dfrac{\tilde{N}(|\mu|)}{\left[\int_{-3}^{\mu} \tilde{N}(|\gamma|)d\gamma\right]^2}, & \frac{1}{4} < \delta < 1, \end{cases} \tag{31}$$

which is proportional to the free DOS. For $U > 0$, κ should evolve simultaneously with the quasiparticle DOS which makes it adequate to indicate the dependence of this quantity upon interaction. The κ's as a function of δ at $U = 0, 2, 4, 6$, and 8 are plotted in Fig. 7. For $U < U_{\mathrm{AFM}}$, the compressibility near the van Hove singularity is suppressed most drastically by interaction, while that at low energy (near the Dirac points) remains very close to the noninteracting one, reflecting that the Dirac cone structure is very robust, and the DOS of the quasiparticles is transferred away from the van Hove singularity as U increases. Furthermore, at $U = 4, 6$, there exhibit a discontinuity at $\delta = \delta_M$ where the AFM to PM phase transition occurs, and the one-sided peak of κ as δ approaches δ_M manifests that the system now is an itinerant AFM metal. However, at $U = 8$, there exist two consecutive discontinuities: (i) between positively and negatively divergent κ; (ii) between negatively divergent and positive small κ.

IV. PHASE DIAGRAM

The staggered magnetization M with U and δ being its parameters is plotted in Fig. 8, where the phase boundary between the AFM and PM states is delineated by $\delta_M(U)$. Obviously, M maximizes at small dopings and large couplings. The phase boundary $\delta_M(U)$ shows a nonmonotonic behavior upon U that may be connected to the crossover of Δ_{AFM} as U increases. We also notice that M saturates when $U > U_{\mathrm{Mott}}$ at small dopings, reflecting that the physical properties in the

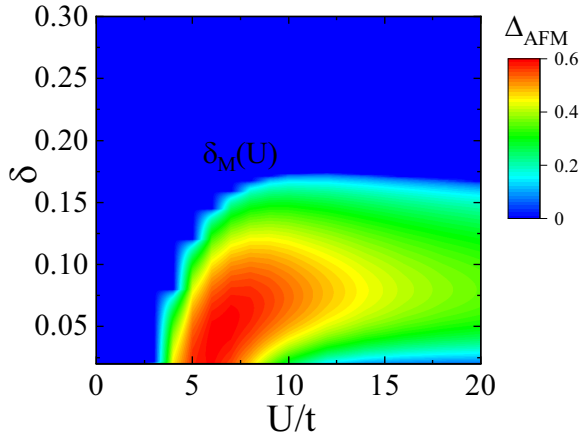

FIG. 9. The AFM gap Δ_{AFM} as function of U and δ obtained by six-site cluster with $\delta_M(U)$ separating the AFM and PM states.

AFM state are dominated by the underlying Mott transition in the half-filled PM state.

The AFM energy gap Δ_{AFM} in the same parameter space is plotted in Fig. 9, where the phase boundary $\delta_M(U)$ still holds, denoting that there are no intermediate states before the semimetal to AFMI transition occurs. An overall crossover between the weak- and strong-coupling regimes can be observed in Δ_{AFM} when U grows, at which Δ_{AFM} reaches its maximum, and the coupling U_c for this crossover is highly δ dependent, in contrast to that in the square lattice case [30]. For $U > U_c$, the maximum of Δ_{AFM} occurs at $\delta \sim 0.075$, leading to an interesting vertical reentrance behavior as δ increases, the same as the square lattice case [30].

Combining Figs. 8–10, an overall phase diagram in the U-δ plane emerges in Fig. 11. In contrast to the square lattice case [30], the crossover U_c in the AFM state at which Δ_{AFM} is maximized, symbolled by the red squares, is shown to be highly δ dependent. On the other hand, U_c at $\delta = 0$ is smaller than U_{Mott} (red triangle), implying that at half filling, the coupling strength separating the weak- and strong-coupling regimes is suppressed by long-range AFM correlations [30]. The blue region in this figure enclosed by $\delta_\kappa^1(U)$ and $\delta_\kappa^2(U)$ is characterized by $M \neq 0$ and $\kappa < 0$ with $\delta_\kappa^1(U)$ being the phase boundary between $M \neq 0$, $\kappa > 0$ and $M \neq 0$, $\kappa < 0$, and $\delta_\kappa^2(U)$ between $M \neq 0$, $\kappa < 0$ and $M = 0$, $\kappa > 0$. The region with $\kappa < 0$ is extremely small compared to the square lattice Hubbard model [30], and exists only in the vicinity of the phase boundary between the AFM and PM state and at intermediate U. It should be noted that the phase diagram has been greatly improved from the two-site to six-site schemes, since in the former case U_{AFM} jumps from $2.75t$ at $\delta = 0$ to $25.5t$ at $\delta = 0.02$, while in the latter it is almost continuous from $2.43t$ to $2.97t$.

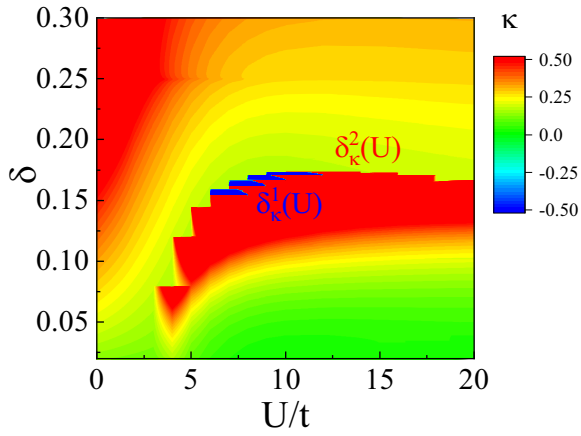

FIG. 10. The compressibility κ as function of U and δ obtained by six-site cluster. The staircase is an artifact because of discrete U's adopted to calculate κ, i.e., $\Delta U = t$ when $U \leqslant 10t$ and $\Delta U = 2t$ when $10t < U \leqslant 20t$, which can only be eliminated in the $\Delta U \to 0$ limit. The blue region between $\delta_\kappa^1(U)$ and $\delta_\kappa^2(U)$ is characterized by $\kappa < 0$, where $\delta_\kappa^1(U)$ and $\delta_\kappa^2(U)$ are delineated by the midpoints of the blue and red steps, respectively. The discontinuities in κ at these two phase boundaries are reflected in the color jumpings.

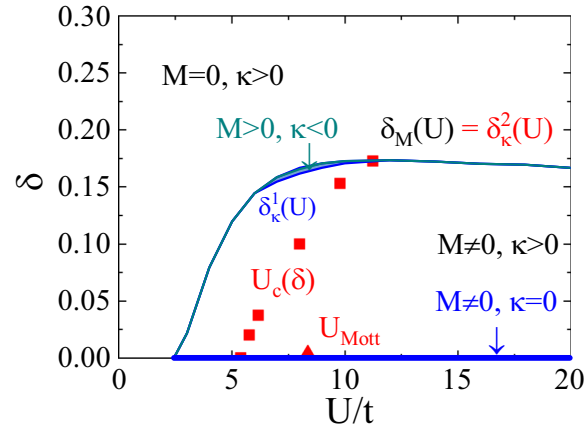

FIG. 11. The U-δ phase diagram of the honeycomb lattice Hubbard model within the six-site cluster scheme. The critical coupling $U_{\mathrm{Mott}} = 8.36t$ for the Mott transition in the half-filled PM state is marked by the red triangle. The crossover coupling $U_c(\delta)$ in the AFM state at $\delta = 0$, 0.02, 0.0375, 0.1, 0.1531, and 0.1725 are symbolized by red squares, at which Δ_{AFM} reaches its maximum. The half-filling case with $U > 2.43t$ is highlighted by the heavy blue line, in which the system is an AFM insulator with $\kappa = 0$.

V. CONCLUSION

We have exploited the cluster slave-spin method to explore extensively the ground state properties of the one-band honeycomb lattice Hubbard model with U and δ as its parameters. At half filling, the first-order semimetal to insulator Mott transition in the PM state is revealed, characterized by discontinuities and hystereses in all quantities at $U_{\mathrm{Mott}} = 8.36t$ [18,21,44]. In the AFM state, a single direct and continuous phase transition between PM semimetal and AFMI at $U_{\mathrm{AFM}} = 2.43t$ is substantiated, which belongs to the Gross-Neveu-Yukawa universality class [9–16,18], precluding the existence of intermediate phases such as a spin liquid state. At finite dopings, an extended crossover is discovered between the weak- and strong-coupling regimes in the AFM state at which the AFM energy gap Δ_{AFM} reaches its maximum, and the AFM within this crossover is driven by both the kinetic

energy and interaction potential gain. The interaction U_c for this crossover is shown to be highly δ dependent, in contrast to the square lattice system where U_c remains almost unchanged with large dopings [30].

Moreover, for the half-filled system, by analytically calculating the relation between M and Δ_{AFM} in the vicinity of PM semimetal to AFM insulator transition, Eq. (28), we found that to the leading order, M is linearly dependent on Δ_{AFM}, compared to the square lattice result that is proportional to $\Delta_{\mathrm{AFM}}(\ln \Delta_{\mathrm{AFM}})^2$ (Ref. [30]). This difference is consistent with the vanishing noninteracting DOS at Dirac points in the honeycomb lattice, in contrast to the van Hove singularity of the free electron DOS at the Fermi surface in a half-filled square lattice.

Finally, an overall phase diagram in the U-δ plane is presented in Fig. 11; the phase boundary $\delta_M(U)$ separating the AFM and PM phases shows a nonmonotonic behavior with the increasing U, which is consistent with the crossover behavior of Δ_{AFM}. The phase boundary between the AFM metal with $\kappa > 0$ and the AFM insulator with $\kappa = 0$ locates exactly at $\delta = 0$. The region with $\kappa < 0$ only exists in the vicinity of the phase boundary between the AFM and PM state and at intermediate coupling strengths, whose area is extremely small compared to the counterpart in the square lattice Hubbard model [30].

It is worth mentioning that though lacking available data from the previous studies to verify our results at finite dopings, we corroborate that there are no intermediate states such as a spin liquid between the PM semimetal and AFMI phases at half filling [9–16,18], and the critical transition exponent of staggered magnetization between these two states is quite close to those from large-scale QMC simulations [9,11,15,17] and density matrix embedding theory calculations [21], which could well justify our calculations. We would like to mention that the interesting physics in the Hubbard model on a honeycomb lattice could be connected with the properties of graphene-based material [40,46–48], and also the optical lattice systems for ultracold atoms [49]. The ionic Hubbard model with ultracold fermions based on the honeycomb lattice has been realized where the transition from metal to charge density wave has been observed, and our theoretical prediction is consistent with the experimental results at the limit of stagger potential equal to zero. We hope our full phase diagram in the parameter space of on-site interaction and doping may simulate further experimental detection on graphene-based material or optical lattice systems for ultracold atoms.

ACKNOWLEDGMENTS

We thank Shiping Feng, Xiong Fan, and Yu Ni for many helpful discussions. One of the authors (M.H.Z.) would like to acknowledge the beneficial communications with Rong Yu. This work was supported by NSFC (Grants No. 11974049 and No. 11774033), Beijing Natural Science Foundation (Grant No. 1192011), and the HSCC program of Beijing Normal University.

[1] J. Hubbard, Proc. R. Soc. London A **276**, 238 (1963); **277**, 237 (1964).
[2] S. R. White, D. J. Scalapino, R. L. Sugar, E. Y. Loh, J. E. Gubernatis, and R. T. Scalettar, Phys. Rev. B **40**, 506 (1989).
[3] M. Qin, T. Schäfer, S. Andergassen, P. Corboz, and E. Gull, arXiv:2104.00064.
[4] Z. Y. Meng, T. C. Lang, S. Wessel, F. F. Assaad, and A. Muramatsu, Nature (London) **464**, 847 (2010).
[5] M. Hohenadler, T. C. Lang, and F. F. Assaad, Phys. Rev. Lett. **106**, 100403 (2011).
[6] M. Hohenadler, T. C. Lang, and F. F. Assaad, Phys. Rev. Lett. **109**, 229902(E) (2012).
[7] M. Hohenadler, Z. Y. Meng, T. C. Lang, S. Wessel, A. Muramatsu, and F. F. Assaad, Phys. Rev. B **85**, 115132 (2012).
[8] D. Zheng, G.-M. Zhang, and C. Wu, Phys. Rev. B **84**, 205121 (2011).
[9] Y. Otsuka, S. Yunoki, and S. Sorella, Phys. Rev. X **6**, 011029 (2016).
[10] M. Raczkowski, R. Peters, T. T. Phùng, N. Takemori, F. F. Assaad, A. Honecker, and J. Vahedi, Phys. Rev. B **101**, 125103 (2020).
[11] F. F. Assaad and I. F. Herbut, Phys. Rev. X **3**, 031010 (2013).
[12] T. Paiva, R. T. Scalettar, W. Zheng, R. R. P. Singh, and J. Oitmaa, Phys. Rev. B **72**, 085123 (2005).
[13] A. Yamada, Int. J. Mod. Phys. B **30**, 1650158 (2016).
[14] S. Sorella and E. Tosatti, Europhys. Lett. **19**, 699 (1992).
[15] S. Sorella, Y. Otsuka, and S. Yunoki, Sci. Rep. **2**, 992 (2012).
[16] J. Ostmeyer, E. Berkowitz, S. Krieg, T. A. Lähde, T. Luu, and C. Urbach, Phys. Rev. B **102**, 245105 (2020).
[17] J. Ostmeyer, E. Berkowitz, S. Krieg, T. A. Lähde, T. Luu, and C. Urbach, Phys. Rev. B **104**, 155142 (2021).
[18] S. R. Hassan and D. Sénéchal, Phys. Rev. Lett. **110**, 096402 (2013).
[19] K. Seki and Y. Ohta, arXiv:1209.2101.
[20] A. Liebsch and W. Wu, Phys. Rev. B **87**, 205127 (2013).
[21] Q. Chen, G. H. Booth, S. Sharma, G. Knizia, and G. K.-L. Chan, Phys. Rev. B **89**, 165134 (2014).
[22] S. Arya, P. V. Sriluckshmy, S. R. Hassan, and A.-M. S. Tremblay, Phys. Rev. B **92**, 045111 (2015).
[23] C. Honerkamp, Phys. Rev. Lett. **100**, 146404 (2008).
[24] S. Raghu, X.-L. Qi, C. Honerkamp, and S.-C. Zhang, Phys. Rev. Lett. **100**, 156401 (2008).
[25] Y. R. Wang, J. Wu, and M. Franz, Phys. Rev. B **47**, 12140 (1993).
[26] S. Feng, J. B. Wu, Z. B. Su, and L. Yu, Phys. Rev. B **47**, 15192 (1993); S. Feng, Z. B. Su, and L. Yu, *ibid.* **49**, 2368 (1994); S. Feng, *ibid.* **68**, 184501 (2003); S. Feng, J. Qin, and T. Ma, J. Phys.: Condens. Matter **16**, 343 (2004); S. Feng, Y. Lan, H. Zhao, L. Kuang, L. Qin, and X. Ma, Int. J. Mod. Phys. B **29**, 1530009 (2015).
[27] S. R. Hassan and L. de' Medici, Phys. Rev. B **81**, 035106 (2010).
[28] R. Yu and Q. Si, Phys. Rev. B **86**, 085104 (2012).
[29] W.-C. Lee and T.-K. Lee, Phys. Rev. B **96**, 115114 (2017).

[30] M.-H. Zeng, T. Ma, and Y.-J. Wang, Phys. Rev. B **104**, 094524 (2021).
[31] Z.-C. Gu, H.-C. Jiang, D. N. Sheng, H. Yao, L. Balents, and X.-G. Wen, Phys. Rev. B **88**, 155112 (2013).
[32] W.-S. Wang, Y.-Y. Xiang, Q.-H. Wang, F. Wang, F. Yang, and D.-H. Lee, Phys. Rev. B **85**, 035414 (2012).
[33] R. Nandkishore, L. S. Levitov, and A. V. Chubukov, Nat. Phys. **8**, 158 (2012).
[34] P. Coleman, Phys. Rev. B **35**, 5072 (1987).
[35] P. A. Lee and N. Nagaosa, Phys. Rev. B **46**, 5621 (1992).
[36] S. Florens and A. Georges, Phys. Rev. B **70**, 035114 (2004).
[37] T. Senthil, Phys. Rev. B **78**, 045109 (2008).
[38] G. Kotliar and A. E. Ruckenstein, Phys. Rev. Lett. **57**, 1362 (1986).
[39] W. Witczak-Krempa, Ph.D. thesis, University of Toronto, 2013.
[40] T. Ma, L. Zhang, C.-C. Chang, H.-H. Hung, and R. T. Scalettar, Phys. Rev. Lett. **120**, 116601 (2018).
[41] N. Bleinstein and R. A. Handelsman, *Asymptotic Expansions of Integrals* (Dover Publications, New York, 1986).
[42] T. Ogawa, K. Kanda, and T. Matsubara, Prog. Theor. Phys. **53**, 614 (1975).
[43] M. Abram, J. Kaczmarczyk, J. Jedrak, and J. Spalek, Phys. Rev. B **88**, 094502 (2013).
[44] M.-T. Tran and K. Kuroki, Phys. Rev. B **79**, 125125 (2009).
[45] D. Vollhardt, Rev. Mod. Phys. **56**, 99 (1984).
[46] I. F. Herbut, Phys. Rev. Lett. **97**, 146401 (2006).
[47] A. H. Castro Neto, F. Guinea, N. M. R. Peres, K. S. Novoselov, and A. K. Geim, Rev. Mod. Phys. **81**, 109 (2009).
[48] T. Ma, F. Hu, Z. Huang, and H.-Q. Lin, Appl. Phys. Lett. **97**, 112504 (2010); T. Ma, Z. Huang, F. Hu, and H.-Q. Lin, Phys. Rev. B **84**, 121410(R) (2011); T. Ma, F. Yang, H. Yao, and H.-Q. Lin, *ibid.* **90**, 245114 (2014).
[49] M. Messer, R. Desbuquois, T. Uehlinger, G. Jotzu, S. Huber, D. Greif, and T. Esslinger, Phys. Rev. Lett. **115**, 115303 (2015).